CONDENSED MATTER PHYSICS

Colossal anisotropic absorption of spin currents induced by chirality

Rui Sun[1,2]†, Ziqi Wang[3,2]†, Brian P. Bloom[4]†, Andrew H. Comstock[1,2], Cong Yang[3,2], Aeron McConnell[1,2], Caleb Clever[4], Mary Molitoris[4], Daniel Lamont[5], Zhao-Hua Cheng[6], Zhe Yuan[7], Wei Zhang[8], Axel Hoffmann[9], Jun Liu[3,2]*, David H. Waldeck[4]*, Dali Sun[1,2]*

The chiral induced spin selectivity (CISS) effect, in which the structural chirality of a material determines the preference for the transmission of electrons with one spin orientation over that of the other, is emerging as a design principle for creating next-generation spintronic devices. CISS implies that the spin preference of chiral structures persists upon injection of pure spin currents and can act as a spin analyzer without the need for a ferromagnet. Here, we report an anomalous spin current absorption in chiral metal oxides that manifests a colossal anisotropic nonlocal Gilbert damping with a maximum-to-minimum ratio of up to 1000%. A twofold symmetry of the damping is shown to result from differential spin transmission and backscattering that arise from chirality-induced spin splitting along the chiral axis. These studies reveal the rich interplay of chirality and spin dynamics and identify how chiral materials can be implemented to direct the transport of spin current.

INTRODUCTION

Spin currents are essential for the development of modern spintronics concepts (*1*). These spin currents and the concomitant transport of angular momentum can come in the form of spin-polarized charge currents, pure spin currents, or magnetic excitations (spin waves). The transport of spin through any of these means can be used to manipulate magnetic states through spin-torques and interrogate the magnetic states via magnetotransport phenomena, thereby laying the foundation for energy-efficient information technologies based on encoding data in nonvolatile magnetization configurations (*2*). Initially, i.e., for the seminal discovery of giant magnetoresistance (*3*, *4*), spin currents were generated from electric currents via exchange interactions, where a ferromagnetic (FM) conductor acts as polarizer for electron spins, similar to concepts familiar from ordinary optics (*5*). Subsequently, spin-orbit torques have been recognized as a more efficient source of spin currents and now are key to next-generation spintronic device developments (*6*). Even more recently, it has been recognized that angular momentum transport may even originate just from the orbital dynamics of electrons (*7*). Toward this end, materials with chiral structures are of increased interest because their electronic properties can naturally have a momentum dependent orbital polarization, which, in turn, can result in intriguing spin generation effects (*8*). Related effects have been termed chiral induced spin selectivity (CISS), but the underlying microscopic physics of CISS is still a matter of active controversy (*9*).

A pure spin current, $\mathbf{J_s}$, is a tensor given by the outer product of two vectors: one is the spin angular momentum (polarization of the spin degree of freedom) $\mathbf{P}_s^{\boldsymbol{i}}$, which is an axial vector, and the other is the translational momentum (a net flow direction of propagating spins) $\mathbf{J}^{\boldsymbol{j}}$, which is a polar vector. Note that *i* and *j* represent the Cartesian coordinates *x*, *y*, and *z*. One basic feature of spintronic devices relies on the detection of $\mathbf{P}_s^{\boldsymbol{i}}$ (up or down) at an electrode terminal. The relative alignment between spin orientation and magnetic moments, the spin up versus spin down states, can be differentiated by interfacing to an adjacent FM layer and measuring the giant magnetoresistance (*3*, *4*). In contrast to the analysis of $\mathbf{P}_s^{\boldsymbol{i}}$, another increasingly compelling strategy is to manipulate the transmission of $\mathbf{Js}$ in nonmagnetic materials (NMs). Such a differentiation of spin state acts like an "on-off switch" for spin-current and can be achieved by harnessing the anisotropic absorption of spin currents during propagation in NMs. This process is akin to gate control of electrical conductivities in Si-based field-effect transistors and holds great potential for designing spin-based transistors.

Spin angular momentum can be transferred from a FM layer into an adjacent NM layer, resulting in a pure spin current flow in the NM. Via spin pumping, the flow of $\mathbf{Js}$ across the FM/NM interface can be probed by examining the phenomenological Gilbert damping factor, α, and it constitutes one of the key parameters describing the dynamics of FM materials and the spin-related characteristics of an adjacent NM (*10*, *11*)

$$\mathbf{J}_s = \frac{\hbar}{4\pi} g^{\uparrow\downarrow} \mathbf{M} \times \frac{d\mathbf{M}}{dt} \text{ and } \alpha = \alpha_0 + g^{\uparrow\downarrow}\gamma\hbar/(4\pi M_s d_{\mathrm{FM}}) \tag{1}$$

where γ is the gyromagnetic ratio, $\hbar$ is the reduced Planck constant, $\mathbf{M}$ is the magnetic moment, M_s is the saturation magnetization, and d_{FM} is thickness of the FM layer. α_0 is the intrinsic Gilbert damping constant of the FM, and $g^{\uparrow\downarrow}$ is the spin mixing conductance, which describes the difference between spin-dependent reflection and transmission coefficients at the FM/NM interface. $g^{\uparrow\downarrow}$ can be cast in terms of an enhancement of the Gilbert damping Δα (i.e., $\Delta\alpha = \alpha - \alpha_0$) (*10*). The magnitude of Δα is typically determined by the material parameters for a prepared FM/NM interface and is isotropic regardless of the spin polarization orientations (see

---

[1] Department of physics, North Carolina State University, Raleigh, NC 27695, USA. [2] Organic and Carbon Electronics Laboratories (ORaCEL), North Carolina State University, Raleigh, NC 27695, USA. [3] Department of Mechanical and Aerospace Engineering, North Carolina State University, Raleigh, NC 27695, USA. [4] Department of Chemistry, University of Pittsburgh, Pittsburgh, PA 15260, USA. [5] Petersen Institute of Nanoscience and Engineering, University of Pittsburgh, Pittsburgh PA 15260, USA. [6] Beijing National Laboratory for Condensed Matter Physics, Institute of Physics, Chinese Academy of Sciences, Beijing 100190, China. [7] Department of Physics, Beijing Normal University, Beijing 100875, China. [8] Department of Physics and Astronomy, University of North Carolina at Chapel Hill, Chapel Hill, NC 27599, USA. [9] Department of Materials Science and Engineering and Materials Research Laboratory, University of Illinois at Urbana-Champaign, Urbana, IL 61801, USA.
*Corresponding author. Email: jliu38@ncsu.edu (J.L.); dave@pitt.edu (D.H.W.); dsun4@ncsu.edu (D.S.)
†These authors contributed equally to this work.

Fig. 1A). On-demand control over the anisotropy of local Gilbert damping α has been realized by rotating the magnetization orientation of the FM, either through the modification of interfacial anisotropic density of states or through variation of spin-orbit coupling (SOC), to affect the anisotropic transmission of spin currents (*12*–*14*). While maximum-minimum anisotropic ratios up to ~400 to 650% have been reported for a local spin state (*13*, *14*), achieving higher anisotropic transmission of nonlocal spin current is desirable.

The connection between the electron spin and chiral symmetry, i.e., the CISS effect, has only begun to emerge into the scientific forefront over the past two decades; however, its implications in biology (*15*), chemistry (*16*, *17*), and physics (*8*, *18*, *19*) promise transformative applications. Chirality, the absence of mirror and inversion

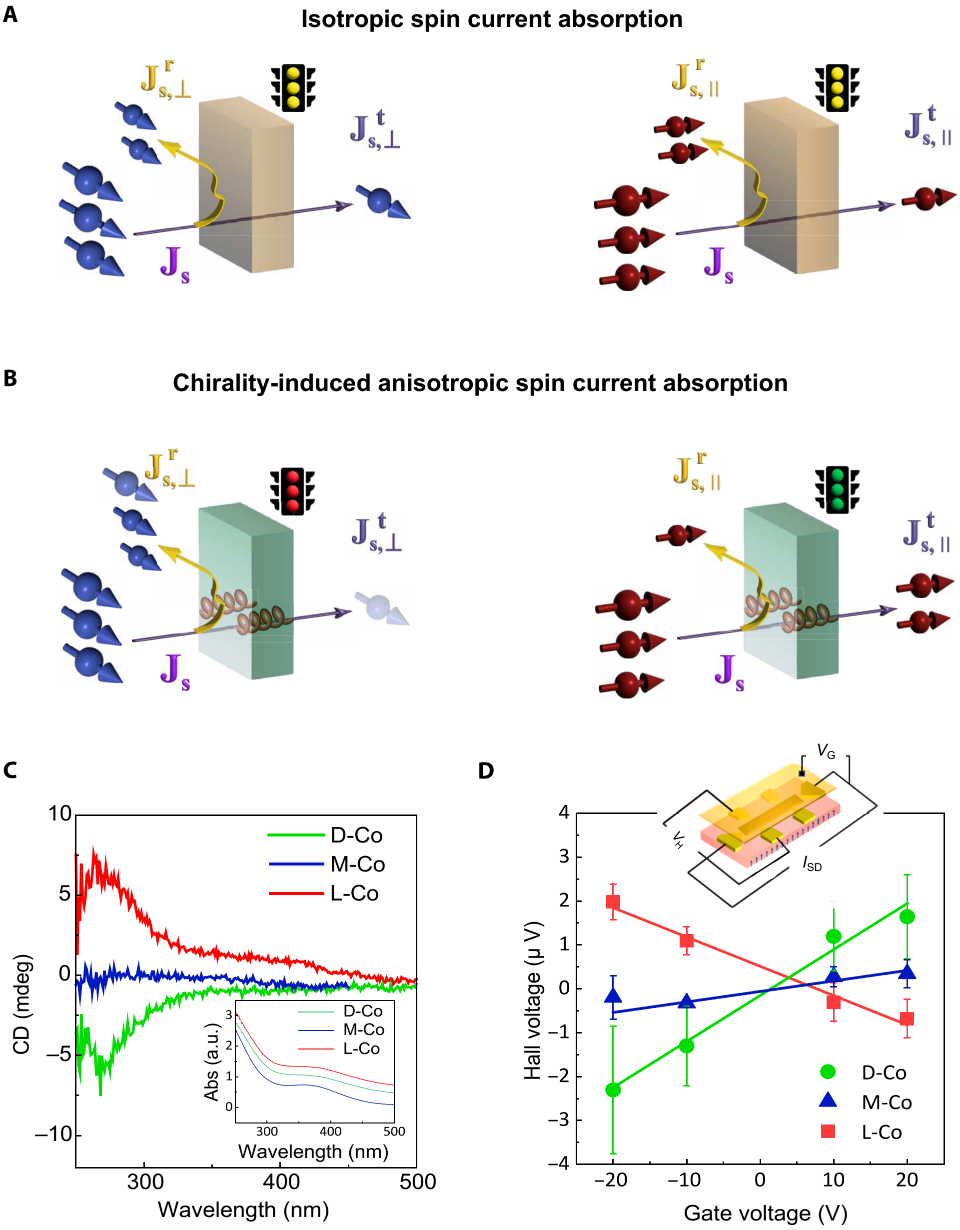

Fig. 1. Schematic diagram of spin current absorption through achiral and chiral channels and properties of L-Co, D-Co, and M-Co thin films. (**A**) In an achiral material, spin current $\mathbf{J_s}$ with spin polarization perpendicular (left) and parallel (right) to *z* flows along the *z* direction. The transmitted spin current $J^t_{s,\parallel}$ and reflected spin current $J^r_{s,\parallel}$ (right of the object) is identical to $J^t_{s,\perp}$ and $J^r_{s,\perp}$ (left of the object), resulting in an isotropic nonlocal Gilbert damping factor in achiral spin channel. (**B**) In a chiral material, $\mathbf{J_s}$ still flows along the *z* direction, which is also the direction of the material's chiral axis. The spin current transmission through the interface with spin polarization parallel to the material's chiral axis is greatly enhanced compared to that with spin polarization perpendicular to the chiral axis, i.e., $J^t_{s,\parallel} \gg J^t_{s,\perp}$, whereas $J^r_{s,\parallel} \ll J^r_{s,\perp}$, resulting in a difference of the enhanced damping factor. (**C**) Circular dichroism (CD) spectra and absorbance (inset) of L-Co, D-Co, and M-Co thin films in arbitrary unit (a.u.). (**D**) A schematic representation of the Hall device measurements and corresponding measured Hall voltages (V_H) as a function of gate voltage (V_G) with a fixed source drain current (I_{SD}) in different cobalt oxide films. The error bars represent the SD of the mean for three independently prepared Hall devices.

symmetry, fundamentally breaks the corresponding symmetries of electronic structure and spin/orbit textures. Recent work suggests that chiral matter displays large effective SOC, beyond that of the atomic spin-orbit interaction commonly probed in spectroscopy, and manifests efficient "spin filtering" when a charge current passes along the chiral axis of materials (*20*, *21*). According to the generalized Landau-Lifshitz-Gilbert equation (*22*, *23*), the Gilbert damping factor is treated as a tensor, implying that control over the rotational or orientational anisotropy could play a crucial role in directing spin current, as shown in Fig. 1B. The combination of structural chirality and enhanced SOC along the chiral axis presents an exciting opportunity to engineer the anisotropy of the Gilbert damping factor through the CISS effect.

Here, we report the emergence of colossal anisotropic absorption of nonlocal spin currents in chiral cobalt oxide thin films. We find that the Gilbert damping in a chiral cobalt oxide film exhibits a maximum (minimum) value when the direction of the spin polarization is parallel (perpendicular) to the chiral axis, whereas an achiral analog of the cobalt oxide film shows isotropic damping. By rotating the magnetization orientation of the FM from the in-plane to the out-of-plane direction, a twofold symmetry of the anisotropic damping manifests and displays a maximum-minimum ratio of 10 times. This effect is attributed to the strong spin-flip process arising from chirality-induced band spin splitting, which yields a reciprocal large spin transmission probability along the chiral axis. These studies reveal a pathway for tailoring anisotropic nonlocal Gilbert damping through structural chirality.

RESULTS

Spin filtering properties of chiral metal oxides

In this work, chiral metal oxide thin films are used to study the anisotropic absorption of spin currents (*24*). Levo–cobalt oxide (L-Co), Dextro–cobalt oxide (D-Co), and achiral, meso–cobalt oxide (M-Co) thin films were prepared by electrodeposition from solutions of their corresponding cobalt tartrate solutions as described previously; see Methods for additional details (*24*, *25*). Figure 1C shows the absorbance (inset) and circular dichroism (CD) spectra measured for the three films. The mirror-image CD response for the L-Co and D-Co films demonstrates control over the chiro-optical response by manipulation of the tartrate's enantiomeric form, whereas the M-Co film displays no CD signal and is achiral. Characterization of the films using x-ray photoelectron spectroscopy, x-ray diffraction, and surface topography measurements indicates that the structural and morphological features of the L-Co and D-Co films are indistinguishable from those of the M-Co, aside from the chiroptical response (see Supplementary Text S1 for experimental details). The spin filtering properties of the chiral oxide films were confirmed by Hall bar measurements. Figure 1D shows the schematic principle of the Hall bar configuration and the corresponding Hall voltages measured under different gate voltages. For the chiral cobalt oxide films, the Hall voltage is linearly proportional to the gate voltage (over the range studied) and exhibits a reversal of polarity for the Hall voltage depending on the enantiomorph (L-Co versus D-Co). No appreciable Hall voltage is detected for the achiral M-Co film. Magnetic conductive atomic force microscopy (mc-AFM) measurements on L-Co and D-Co further corroborate the Hall measurements (see Supplementary Text S2). Collectively, the CD, Hall bar, and mc-AFM measurements confirm the structural chirality of the prepared cobalt oxide thin films and the corresponding spin-dependent electron transmission arising from the CISS effect.

Colossal anisotropic absorption of spin current

We performed the FM resonance (FMR) spectroscopy to characterize the absorption of pure spin current by chiral metal oxides in proximity to a FM layer by spin pumping. Three types of $Ni_{81}Fe_{19}$ (NiFe)/Cu/cobalt oxide heterostructures were prepared: (i) a chiral heterostructure, $Ni_{81}Fe_{19}$(15 nm)/Cu(50 nm)/L-Co(25 nm) (NiFe/Cu/L-Co); (ii) an achiral heterostructure, $Ni_{81}Fe_{19}$(15 nm)/Cu(50 nm)/Meso-Co(25 nm) (NiFe/Cu/M-Co); and (iii) a control sample, $Ni_{81}Fe_{19}$(15 nm)/Cu(50 nm)/glass substrate (see Methods). A 50-nm-thick Cu spacer layer is inserted to act as a spin transport channel between the $Ni_{81}Fe_{19}$ and cobalt oxides while excluding any possible proximity effects (*26*). A schematic diagram of the FMR measurement geometry is shown in Fig. 2A. In the FMR measurements, a microwave field with a fixed frequency, f ($f = \omega/2\pi$), is transmitted through a high bandwidth waveguide and excites the NiFe layer, whereas a magnetic field, H, is swept across the resonance condition. Under the FMR condition, the magnetization precession of the NiFe layer generates a pure spin current, which propagates through the Cu spacer layer and interacts with the cobalt oxide layer. A derivative absorption profile for the NiFe resonance as a function of H (modulated FMR) represents the nonlocal spin current absorbed by the adjacent Cu/cobalt oxide layer. Figure 2B plots the H-dependent FMR spectra for the NiFe/Cu/L-Co (red), NiFe/Cu/M-Co (blue), and NiFe/Cu (green) samples at $f = 6$ GHz and magnetic field angle with respect to the z axis, $\theta_H = 90°$, and the resonance field and full-width-at-half-maximum linewidth, ΔH, were extracted from the spectra. The chiral NiFe/Cu/L-Co exhibits a broader FMR linewidth compared to that of the achiral NiFe/Cu/M-Co and NiFe/Cu, indicating that enhanced spin current dissipation arises from the chiral oxide films upon spin pumping (*27*). When the magnetization of the NiFe is rotated toward the chiral axis of the cobalt chiral film (at $\theta_H = 45°$, see Fig. 2C), a much broader FMR linewidth of the chiral NiFe/Cu/L-Co (red) is observed, in sharp contrast to the moderately increased linewidths for the achiral NiFe/Cu/M-Co (blue) and NiFe/Cu (green) control samples. Figure 2D plots the linewidth, $\mu_0\Delta H$, obtained for NiFe/Cu/L-Co (left), NiFe/Cu/M-Co (right, top), and NiFe/Cu (right, bottom) as a function of microwave frequency at different θ_H, respectively. The relationship between $\mu_0\Delta H$ and f can be described by (*28*)

$$\mu_0\Delta H = \frac{\alpha\gamma\left(F_{\theta\theta} + \frac{1}{\sin^2\theta}F_{\varphi\varphi}\right)}{M_s\,|d\omega/dH|} + \mu_0\Delta H_0 \tag{2}$$

where F_{ij} denotes the coefficient of the parabolic approximation for the free energy (see Supplementary Text S4), and $\mu_0\Delta H_0$ is the inhomogeneous broadening linewidth caused by sample roughness, defects, or orientation of crystallites. For a magnetic system without strong magnetic anisotropy and anisotropic damping factor, the Gilbert damping α is proportional to the slope of $\mu_0\Delta H$ versus f, i.e., $\mu_0\Delta H = \frac{4\pi\alpha}{\gamma}f + \mu_0\Delta H_0$. For the NiFe/Cu/L-Co sample at $\theta_H = 90°$, according to the linear fit, $\alpha(L - Co, 90°) = 0.033$ and is ~3 times larger than that for the NiFe/Cu/M-Co sample, $\alpha(M - Co, 90°) = 0.0132$. The parameter $\alpha(90°)$ is the summation of the intrinsic Gilbert damping of NiFe and the conventional nonlocal Gilbert

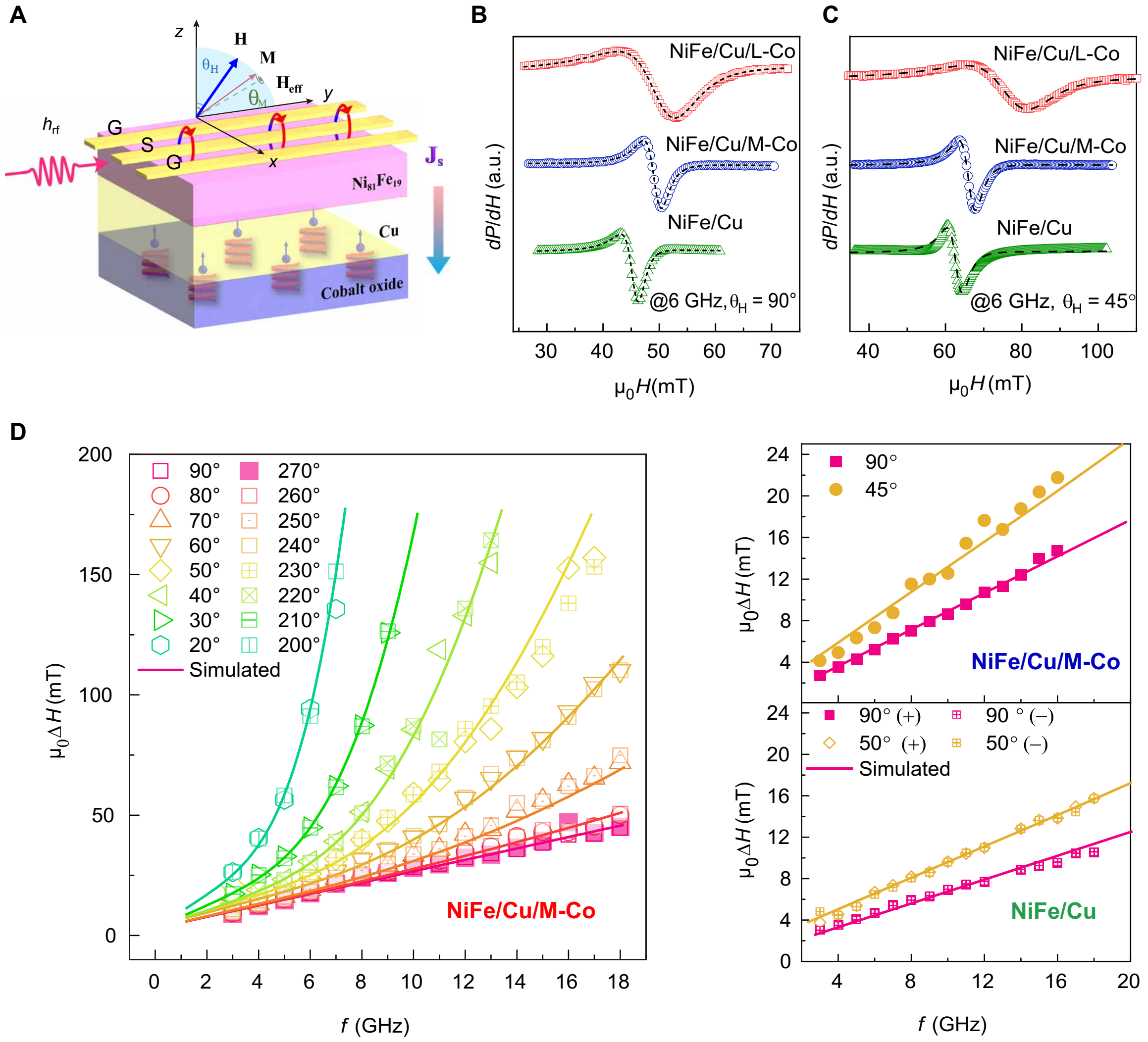

Fig. 2. Spin current transport in chiral and achiral channel characterized by FMR. (**A**) Schematic of the FMR measurements in which the microwave transmits through the planar waveguide, and a radio-frequency field with a frequency *f* excites the magnetization dynamics. A pure spin current diffuses from the FM, through the Cu layer, and then into the metal oxide. (**B**) Representative FMR spectra for NiFe/Cu/L-Co (red), NiFe/Cu/M-Co (blue), and NiFe/Cu (green) measured at 6 GHz with $\theta_H = 90°$. The dashed curve is a fit according to eq. S4 (Supplementary Text). (**C**) The *f*-dependent $\mu_0\Delta H$ for NiFe/Cu/L-Co, NiFe/Cu/M-Co, and NiFe/Cu at $\theta_H = 45°$. (**D**) Field angle θ_H and frequency dependence of linewidth for NiFe/Cu/L-Co (left). The measurements are conducted with θ_H varied from 90° to 20° and 270° to 200°. The right panel shows the linear ΔH versus *f* in NiFe/Cu/M-Co and NiFe/Cu, which are both achiral, systems when the magnetic field is in-plane and tilted out-of-plane. All of the solid curves are a fit to the data using global analysis.

damping. When H is tilted out-of-plane, $\mu_0\Delta H$ of the NiFe/Cu/M-Co and NiFe/Cu control samples remain linearly proportional to *f* (see right panels in Fig. 2D). A slight increase of the slope in achiral and control samples is expected due to magnetic mosaicity. Unexpectedly, $\mu_0\Delta H$ versus *f* in the NiFe/Cu/L-Co sample is nonlinear, and $\mu_0\Delta H$ increases markedly at higher microwave frequencies. The nonlinearity becomes more pronounced as the applied field angle approaches the out-of-plane direction, i.e., the chiral axis of the metal oxide, and it results in a "colossal" anisotropy in the damping that is orders of magnitude different with respect to the chiral axis. Here, measured $\mu_0\Delta H$ in the NiFe/Cu/L-Co sample can exceed 150 mT at $f = 6$ GHz and $\theta_H = 40°$. This conclusion was corroborated through a vector network analyzer under the same FMR conditions (Supplementary Text S5). It is also noteworthy that $\mu_0\Delta H$ versus *f* shows a similar nonlinearity when the applied field direction is inverted ($+H$ or $-H$), which implies that the nonlinear damping is not selective to the injected spin polarization being parallel or antiparallel to the chiral axis.

Time-resolved magnetic-optical Kerr effect

Whereas the FMR measurements show the θ_H dependence for the anisotropic damping factor in the NiFe/Cu/L-Co sample, the large increase in linewidth at lower field angles ($\theta_H < 40°$) makes its estimation by the FMR technique challenging. Thus, we performed time-resolved magnetic-optical Kerr effect (TR-MOKE) measurements in a polar MOKE configuration to investigate the anisotropy of the damping factor at lower field angles. Figure 3A shows a schematic representation of the TR-MOKE measurement in which a

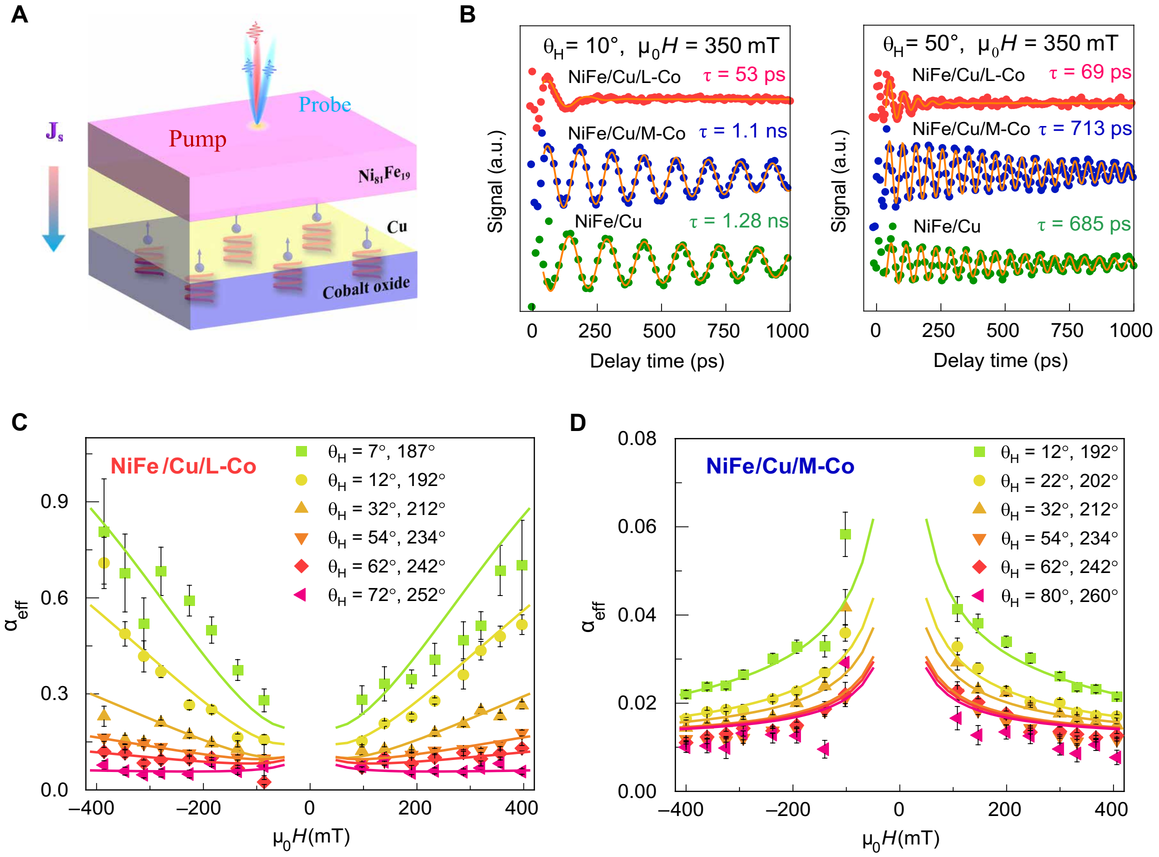

Fig. 3. Spin current transport revealed by TR-MOKE. (**A**) Schematic diagram of the measurement geometry using the pump-probe time-resolved magnetic-optical Kerr effect (TR-MOKE) technique. The pump laser pulse (red) excites the magnetization and is then probed by a delayed laser pulse (blue). A pure spin current diffuses from the NiFe layer, through the copper, and into the metal oxide. (**B**) TR-MOKE signal for NiFe/Cu/L-Co (red), NiFe/Cu/M-Co (blue), and NiFe/Cu (green) measured with $H = 350$ mT for $\theta_H = 10°$ (left) and $\theta_H = 50°$ (right). The solid lines are fits to the data using eq. S6 (Supplementary Text). The extracted effective damping factor α_{eff} as a function of $\pm H$ with varied θ_H for NiFe/Cu/L-Co (**C**) and NiFe/Cu/M-Co (**D**), respectively. The solid lines are simulated global fits to the data.

femtosecond laser pulse initiates precession of the magnetization vector, i.e., magnetization precession, in the NiFe layer. Figure 3B (left) shows the measured magnetization dynamics for the NiFe/Cu/L-Co (red), NiFe/Cu/M-Co (blue), and NiFe/Cu control (green) with a 350-mT applied magnetic field at $\theta_H = 10°$. A prominent large damping for NiFe/Cu/L-Co occurs, with dynamics ceasing after ~1 period (~53 ps), whereas the oscillations in the NiFe/Cu/M-Co and NiFe/Cu persist for over 1 ns. Figure 3B (right) shows the case of $\theta_H = 50°$ at which the TR-MOKE signal of the NiFe/Cu/M-Co and NiFe/Cu displays a relatively long-lived precession with a magnetization relaxation time, τ, of 775 and 685 ps, respectively. In contrast, the signal of the chiral NiFe/Cu/L-Co sample dampens over an order of magnitude faster, within ~69 ps. This difference in behavior between NiFe/Cu/L-Co and NiFe/Cu/M-Co and NiFe/Cu samples suggests that chirality strongly influences the magnetic dynamics and dissipation at the NiFe/Cu/L-Co interface. The resonance frequency, *f*, increases with the magnetic field strength for both the NiFe/Cu/M-Co and NiFe/Cu/L-Co samples and can be described by the Kittel equation (see fig. S11) (*28*, *29*).

To further characterize differences in the magnetization dynamics arising from the presence of structural chirality, the effective damping factor, α_{eff}, and the Gilbert damping factor, α, were extracted from the relaxation time, τ, through Eq. 3 (see Supplementary Texts S4 and S6) (*29*, *30*)

$$\alpha_{\mathrm{eff}} = \frac{1}{2\pi f \tau} \text{ and } \alpha = \frac{4\pi M_s f}{\gamma\left(F_{\theta\theta} + \frac{1}{\sin^2\theta_H} F_{\varphi\varphi}\right)} \alpha_{\mathrm{eff}} \qquad (3)$$

Figure 3 (C and D) shows the dependence of α_{eff} on the applied external magnetic field strength $\mu_0 H$, at different θ_H values for NiFe/Cu/L-Co and NiFe/Cu/M-Co, respectively. At low external fields, the in-plane demagnetization field, $\mu_0 M_s$, leads to a larger misalignment between the magnetic moment and the applied external magnetic field, giving rise to a larger α_{eff}. As **H** increases, **M** tilts toward **H** so that α_{eff} approaches α, as shown by the data in Fig. 3D (*31*). The value of α in the NiFe/Cu/M-Co sample is ~0.013, only slightly larger than that of the NiFe/Cu control sample, ~0.008 (see fig. S11), and is consistent with the FMR results. Conversely, α_{eff} for the NiFe/Cu/L-Co sample is much larger than that of the NiFe/Cu/M-Co. When θ_H is >70°, α_{eff} in the NiFe/Cu/L-Co sample decreases with increasing **H**, but α_{eff} markedly increases with increasing **H** as the external field is tilted out-of-plane along the chiral axis of the metal oxide. At $\theta_H = 10°$, an ~4 times increase in α_{eff} is observed when the external field is increased from 100 to 400 mT, without showing any saturation. The anomalous field dependent α_{eff} for the chiral NiFe/Cu/L-Co differs from that reported in heavy metal and topological materials with strong SOC (*32–34*). The observed increase of α_{eff} with applied field sharply contrasts with the nonlinearity reported for two-magnon scattering (*35*), in which α_{eff} is suppressed as the magnetization is tilted out-of-plane and greatly diminished when $\theta_M < 45°$ (*36*). Furthermore, the strength of two-magnon scattering decreases as the magnetic field increases, resulting in either a saturation or diminishing dependence of α on the applied field (*36*), in contrast to our observations. Other extrinsic effects, such as drag arising from magnetic anisotropy or mosaicity induced broadening can also be excluded because of the increasing slope of ΔH versus f shown in the FMR measurements.

Twofold symmetry of anisotropic damping

Both TR-MOKE and FMR measurements unambiguously demonstrate the presence of the colossal anisotropic damping factor that changes as a function of the spin polarization's alignment with the chiral axis in the NiFe/Cu/L-Co sample. To quantify the anisotropic damping in the NiFe/Cu/L-Co sample, the Gilbert damping factor, α is expressed as

$$\alpha = \alpha' + \lambda \cos^2\theta_M \tag{4}$$

where θ_M is the magnetization angle of the FM (the change in θ_M as a function of applied field $\mathbf{H}$ and angle θ_H are shown in fig. S5B). α′ is the summation of intrinsic Gilbert damping of NiFe and the "conventional" nonlocal Gilbert damping caused by the spin pumping in the metal oxide, both of which have no angular dependence (*37*); and the term proportional to λ term parameterizes how the anomalous damping depends on the angle. The angle dependence of the damping factor α for the three samples is plotted in Fig. 4. The NiFe/Cu (green) and NiFe/Cu/M-Co (blue) samples both exhibit isotropic α with respect to θ_M (Fig. 4A), whereas α in the NiFe/Cu/L-Co (red) sample is strongly anisotropic (Fig. 4B). A global fitting analysis of the FMR data for the NiFe/Cu/L-Co sample through Eqs. 2 to 4 gives values of α′ ~ 0.033 and λ = 0.95 ± 0.1. Similarly, global fitting of the TR-MOKE data provides α′ ~ 0.035 and λ = 0.9 ± 0.1. Here, the anisotropy of damping factor is defined as $A \equiv \frac{\alpha(\theta_M)}{\alpha(\theta_M = 90^\circ)}$. A theoretical maximum anisotropic ratio, $A_{fit} = \frac{\alpha(\theta_M = 0^\circ)}{\alpha(\theta_M = 90^\circ)} \sim 3000\,\%$ could be achieved according to the fitted parameters from Eq. 4. From the obtained FMR data for the NiFe/Cu/L-Co sample, α has a minimum value at $\theta_M = 90°$ (0.033) and a maximum value at $\theta_M = 65°$ (~0.328), resulting in the measured colossal anisotropic ratio, $A_{exp} = \frac{\alpha(\theta_M = 65^\circ)}{\alpha(\theta_M = 90^\circ)} \sim 1000\,\%$.

DISCUSSION

At $\theta_M = 90°$, an extra enhancement of α in the chiral sample compared to that in the achiral sample can be understood through the spin pumping effect in which chirality-enhanced effective SOC

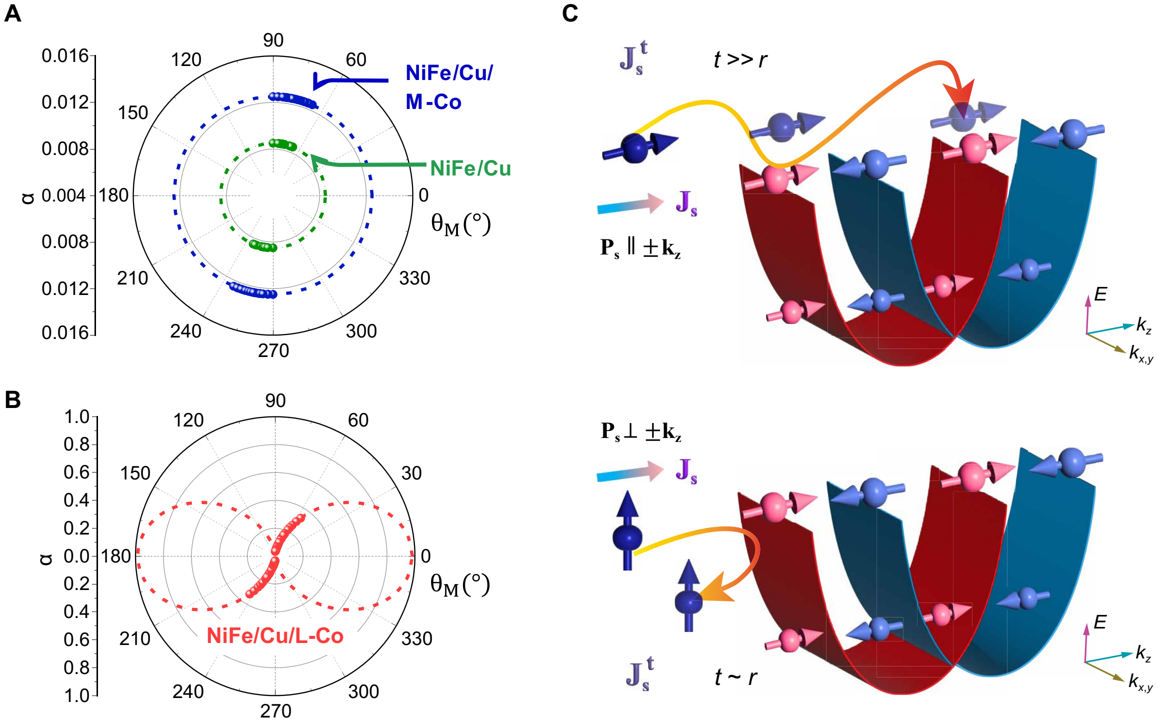

Fig. 4. Anisotropy of nonlocal Gilbert damping factor from chirality selective spin absorption. Comparison of angle-dependent intrinsic damping factor, α, in NiFe/Cu (green) and NiFe/Cu/M-Co (blue) (**A**) and chiral NiFe/Cu/L-Co (red) (**B**) systems. The damping factor α at different θ_M are derived from the globally fitted data using Eqs. 2 and 3 from FMR and TRMOKE approaches. The presented value is the obtained maximum damping factor at this field angle θ_H. (**C**) Schematic representation of spin splitting bands from chirality induced unconventional SOC. The spin states in the electronic structure are either parallel or antiparallel to the chiral axis direction in chiral NiFe/Cu/L-Co. When $\mathbf{P_s} \| \mathbf{k_z}$, electron spins are transmitted into the metal oxide and less are reflected back because of the presence of appropriate spin states. The spin current dissipating in the metal oxide leads to giant Gilbert damping factor. However, when $\mathbf{P_s} \perp \mathbf{k_z}$, the opposite is true.

occurs, similar to the geometric curvature induced SOC reported for C_{60} (*38*). However, the twofold symmetry of the anisotropic damping factor, $\lambda\cos^2\theta_M$, cannot simply be attributed to anisotropic SOC emanating from the chiral metal oxide. Moreover, in contrast to the $\sin^2\theta_M$ dependence of a spin transfer torque model between the FM and spin sink layer (*39*), here, we observe a $\Delta\alpha \propto \cos^2\theta_M$ dependence. Therefore, we attribute the observed colossal anisotropic damping from nonlocal spin current absorption, shown in Fig. 4B, to the CISS effect.

Consider a classic solenoid model in which a charge current induces a magnetic field up to several tesla (*40*). The effective magnetic field induced by the structural chirality can then select for a spin current with a spin polarization aligned with the field and suppress the spin polarization perpendicular to the field. This picture corroborates the emergence of a chirality-induced unconventional SOC in chiral molecules (*41*), which leads to a splitting of the spin-degenerate continuum electronic band (Fig. 4C) into two sub-bands that are shifted with respect to each other in the $\mathbf{k}_z$ direction (i.e., the chiral axis of the metal oxide). These two sub-bands share similar energy dispersion but have opposite spin polarization states due to time reversal symmetry. The spin polarization is oriented either parallel or antiparallel to $\mathbf{k}_z$ due to the one-dimensional parallel spin-momentum locking from chirality induced unconventional SOC (*41*). Because the preservation of time reversal symmetry exists in a chiral system, it leads to an equivalent pure spin current absorption for the spin-up and spin-down in k_z-dependent spin splitting bands. This pure spin transport in chiral materials should be distinguished from the common CISS demonstrations in which the structural chirality induces the electron-to-spin conversion, leading to a preferred spin orientation depending on the handedness.

The precession of the magnetization in the NiFe layer generates pure spin current, $\mathbf{J_s}$, which transmits through the Cu layer and dissipates in the metal oxide layer via a spin-flip process modulated by the chirality-induced unconventional effective SOC. When the injected spin polarization $\mathbf{P_s}$ is parallel to $\pm\mathbf{k}_z$, the spin current is largely absorbed by one of the two split bands; see the top panel of Fig. 4C; i.e., $t \gg r$ (t is the spin transmission probability across the Cu/L-CoO$_x$ interface, and r is the spin reflection probability of the Cu/L-CoO$_x$ interface). The transmitted spin current, $\mathbf{J}_\mathbf{s}^\mathbf{t}$, is large, whereas the reflected spin current from spin backflow, $\mathbf{J}_\mathbf{s}^\mathbf{r}$, is small, resulting in notable damping of the precession in the FM layer. Conversely, when $\mathbf{P_s}$ is perpendicular to $\pm\mathbf{k}_z$ (Fig. 4C, bottom), the influence of chirality on the spin selectivity is negligible, i.e., $t \sim r$ and more closely mimics that of an achiral system. In the context of spin pumping, t and r are proportional to $\mathbf{P_s}\bullet\mathbf{k}_z$, and, thus, the spin current dissipation torque scales with $|t|^2 - |r|^2$ (*10*, *42*–*44*). The behavior is thus expressed as an angle-dependent damping factor term, $\Delta\alpha \propto \lambda\cos^2\theta_M$, as shown in Eq. 4. It is important to note that differences in the damping anisotropy for cobalt oxide having opposite handedness are negligible (see fig. S8), whereas substantial difference appears between the chiral and achiral sample (i.e., M-Co sample). Such behavior further validates the physical origin of anisotropic absorption of spin currents induced by chirality.

The observed colossal anisotropy of spin current absorption in the chiral NiFe/Cu/L-Co heterostructures is unprecedented and sharply contrasts the expected response for a magnetic multilayer system (*43*–*46*). In previous reports, anisotropic damping factors have been shown to arise from interfacial SOC effects or bulk crystalline anisotropy (*12*–*14*, *47*), and the anisotropic damping factor has reached values as high as ~400 to 650% for single-crystal CoFeB(001) films, with a maximum damping factor of ~0.03 (*13*, *14*). However, such an anisotropic damping in CoFeB films results from the magnetic layer itself, i.e., the intrinsic damping factor of the local magnetic moment, not from nonlocal spin current transmission. Although nonlocal anisotropic damping factors related to spin current transmission have been presented (*48*–*51*), the anisotropic ratio is less than 100%. For the NiFe/Cu/L-Co heterostructures investigated here, the chirality-induced nonlocal spin current propagation gives rise to an anisotropy in the Gilbert damping factor that is ~30 times larger (theoretically ~3000%) and displays a maximum damping factor of 0.328 (measured value). This improvement is attributed to chirality-induced spin splitting of spin states, in which the chiral principal axis of the material affords spin selective transmission. Particularly, our results favor a "spin-polarizer" model as a possible mechanism of the CISS effect rather than a "spin-filter" in the presence of pure spin current injection into the chiral materials (*52*). A combination of TR-MOKE and FMR measurements provides crucial and complementary information on the pure spin current generation and magnetization dynamics of chiral materials. The substantial tunability of the nonlocal damping factor heralds a paradigm shift in design strategies for improving the performance of spin memory devices, i.e., faster magnetic switching and larger spin injection efficiency for next-generation spintronic applications, such as spin field-effect transistors and spintronic terahertz emitters.

METHODS

Electrodeposition and characterization of chiral cobalt oxide thin films

Chiral cobalt oxide thin films were prepared by using an electrodeposition method following a previously reported procedure (*24*). Briefly L- or D-tartaric acid (0.8 mmol) and $CoCl_2.6H_2O$ (0.08 mmol) were added to 10 ml of water to make a Co-tartrate complex. Next, sodium carbonate (2 mmol) was added to the solution, and the total volume was increased to 20 ml. A three-electrode system was used in which the counter electrode was a Pt sheet, the reference electrode was Ag/AgCl, and the working electrode comprised 10- to 80-nm Au/5- to 10-nm Ti on a glass, quartz, or silicon wafer substrate. Before the electrodeposition, the substrate was cleaned by placing it in boiling acetone and ethanol for 10 min each, and, then, it was rinsed with water and dried using argon. The electrodeposition was performed at a 0.7-V constant potential for a fixed amount of time until an ~25-nm-thick film was formed. Note that, for thicker films, a longer deposition time was used.

Hall effect device

Hall effect measurements were performed using devices comprising a GaN/AlGaN two-dimensional electron gas (2DEG) capped with a 5-nm gold layer (*53*). The surface was cleaned by heating in 1-methyl-2-pyrilidone at 80°C for 5 hours. A polydimethylsiloxane electrochemical cell was assembled around the device and cured for 18 hours at 45°C. Next a thin film (20 to 25 nm) of chiral cobalt oxide was deposited on the device's Hall bar using electrodeposition. For the deposition, a three-electrode setup was used, where the Au layer on the Hall device acts as the working electrode and Ag and Pt wires were used as the reference and counter electrodes, respectively.

For Hall effect measurements, a cobalt oxide–coated Hall device was placed in an inert electrolyte (0.1 M KCl solution in water) and biased at a voltage with respect to a counter/gate electrode (80-nm Au evaporated onto a 0.2-mm-thick glass coverslip). Buried in the working electrode is a Hall circuit that senses the magnetization induced on the electrode surface. During the measurement, a constant current of 50 μA is driven through the 2DEG channel and a polarizing voltage is applied by a gate electrode using a Keithley 2636B Source Meter, and the Hall effect voltage was measured using a Keithley 2181A Nanovoltmeter. The measurement proceeds by applying a bias voltage between the working electrode and the counter electrode while the voltage between the Hall electrodes within the internal circuit is monitored. The gate voltage, using an Au film, generates a charge polarization in the cobalt oxide layer and, because of the CISS effect, generates a magnetization that is sensed by the Hall bar circuit. Figure S2 shows a representative measurement of a Hall voltage response arising from the application of a fixed gate voltage for L-Co and D-Co samples, and the Hall response as a function of gate voltage is shown in Fig. 1D. Each data point represents the average of multiple measurements of each device as a function of the gate voltage and replicate measurements on multiple devices.

FMR measurement

For the FMR measurements, the NiFe/Cu/L-Co, NiFe/Cu/M-Co, and NiFe/Cu are mounted to the waveguide of a commercially available FMR (NanOsc). To improve the signal-to-noise ratio, the magnetic field is modulated using a Helmholtz coil supplied with a voltage generated from an SR 830 reference output. The reference signal driving the Helmholtz coil uses a 233-Hz frequency. A Keysight EXG Analog Signal Generator N5173B was used as a microwave power source with an amplitude of 0 dBm and frequencies between 3 and 18 GHz. The modulated signal was intercepted by a Krytar microwave power detector model 201B and then was input to SR 830 Lock-in amplifier.

Time-resolved magneto-optical Kerr effect

In the TR-MOKE measurements, a mode-locked Tsunami Ti:Sapphire laser (Spectra Physics) produces a train of pulses at a repetition rate of 80 MHz with a temporal pulse width of 250 fs and a center wavelength of 785 nm with a full width at half maximum ~ 10 nm. The laser is separated into pump and probe beams with orthogonal linear polarizations by a polarizing beam splitter. A mechanical delay stage is used to produce a delay time between the pump beam and probe beam. The reflected linearly polarized probe is split into two orthogonal polarizations with a Wollaston prism. The changes of the polarization on reflection from the sample are measured by the changes in the intensity of the two orthogonal polarization states with a balanced detector. Further details on TR-MOKE can be found in Supplementary Text S6.

Supplementary Materials

This PDF file includes:

Supplementary Texts S1 to S7
Figs. S1 to S12
Legends for data S1 and S2
References

Other Supplementary Material for this manuscript includes the following:

Data S1 and S2

REFERENCES AND NOTES

1. A. Hoffmann, S. D. Bader, Opportunities at the frontiers of spintronics. *Phys. Rev. Appl.* **4**, 047001 (2015).
2. J. Puebla, J. Kim, K. Kondou, Y. Otani, Spintronic devices for energy-efficient data storage and energy harvesting. *Comm. Mater.* **1**, 24 (2020).
3. M. N. Baibich, J. M. Broto, A. Fert, F. Nguyen Van Dau, F. Petroff, P. Etienne, G. Creuzet, A. Friederich, J. Chazelas, Giant magnetoresistance of (001)Fe/(001)Cr magnetic superlattices. *Phys. Rev. Lett.* **61**, 2472–2475 (1988).
4. G. Binasch, P. Grünberg, F. Saurenbach, W. Zinn, Enhanced magnetoresistance in layered magnetic structures with antiferromagnetic interlayer exchange. *Phys. Rev. B* **39**, 4828–4830 (1989).
5. E. Hecht, *Optics* (Pearson education India, 2012).
6. Q. Shao, P. Li, L. Liu, H. Yang, S. Fukami, A. Razavi, H. Wu, K. Wang, F. Freimuth, Y. Mokrousov, M. D. Stiles, S. Emori, A. Hoffmann, J. Akerman, K. Roy, J.-P. Wang, S.-H. Yang, K. Garello, W. Zhang, Roadmap of spin–orbit torques. *IEEE Trans. Magn.* **57**, 1–39 (2021).
7. D. Lee, D. Go, H.-J. Park, W. Jeong, H.-W. Ko, D. Yun, D. Jo, S. Lee, G. Go, J. H. Oh, K.-J. Kim, B.-G. Park, B.-C. Min, H. C. Koo, H.-W. Lee, O. Lee, K.-J. Lee, Orbital torque in magnetic bilayers. *Nat. Commun.* **12**, 6710 (2021).
8. S.-H. Yang, R. Naaman, Y. Paltiel, S. S. P. Parkin, Chiral spintronics. *Nat. Rev. Phys.* **3**, 328–343 (2021).
9. F. Evers, A. Aharony, N. Bar-Gill, O. Entin-Wohlman, P. Hedegard, O. Hod, P. Jelinek, G. Kamieniarz, M. Lemeshko, K. Michaeli, V. Mujica, R. Naaman, Y. Paltiel, S. Refaely-Abramson, O. Tal, J. Thijssen, M. Thoss, J. M. van Ruitenbeek, L. Venkataraman, D. H. Waldeck, B. Yan, L. Kronik, Theory of chirality induced spin selectivity: Progress and challenges. *Adv. Mater.* **34**, e2106629 (2022).
10. Y. Tserkovnyak, A. Brataas, G. E. Bauer, Enhanced gilbert damping in thin ferromagnetic films. *Phys. Rev. Lett.* **88**, 117601 (2002).
11. Y. Tserkovnyak, A. Brataas, G. E. W. Bauer, B. I. Halperin, Nonlocal magnetization dynamics in ferromagnetic heterostructures. *Rev. Mod. Phys.* **77**, 1375–1421 (2005).
12. L. Chen, S. Mankovsky, S. Wimmer, M. A. W. Schoen, H. S. Körner, M. Kronseder, D. Schuh, D. Bougeard, H. Ebert, D. Weiss, C. H. Back, Emergence of anisotropic Gilbert damping in ultrathin Fe layers on GaAs(001). *Nat. Phys.* **14**, 490–494 (2018).
13. Y. Li, F. Zeng, S. S. Zhang, H. Shin, H. Saglam, V. Karakas, O. Ozatay, J. E. Pearson, O. G. Heinonen, Y. Wu, A. Hoffmann, W. Zhang, Giant anisotropy of Gilbert damping in epitaxial CoFe films. *Phys. Rev. Lett.* **122**, 117203 (2019).
14. H. Xu, H. Chen, F. Zeng, J. Xu, X. Shen, Y. Wu, Giant anisotropic Gilbert damping in single-crystal Co-Fe-B(001) films. *Phys. Rev. Appl.* **19**, 024030 (2023).
15. R. Naaman, Y. Paltiel, D. H. Waldeck, Chiral induced spin selectivity and its implications for biological functions. *Annu. Rev. Biophys.* **51**, 99–114 (2022).
16. R. Naaman, Y. Paltiel, D. H. Waldeck, Chiral molecules and the electron spin. *Nat. Rev. Chem.* **3**, 250–260 (2019).
17. R. Naaman, Y. Paltiel, D. H. Waldeck, Chiral induced spin selectivity gives a new twist on spin-control in chemistry. *Acc. Chem. Res.* **53**, 2659–2667 (2020).
18. R. Naaman, D. H. Waldeck, Spintronics and chirality: Spin selectivity in electron transport through chiral molecules. *Annu. Rev. Phys. Chem.* **66**, 263–281 (2015).
19. G. Chang, B. J. Wieder, F. Schindler, D. S. Sanchez, I. Belopolski, S. M. Huang, B. Singh, D. Wu, T. R. Chang, T. Neupert, S. Y. Xu, H. Lin, M. Z. Hasan, Topological quantum properties of chiral crystals. *Nat. Mater.* **17**, 978–985 (2018).
20. R. Nakajima, D. Hirobe, G. Kawaguchi, Y. Nabei, T. Sato, T. Narushima, H. Okamoto, H. M. Yamamoto, Giant spin polarization and a pair of antiparallel spins in a chiral superconductor. *Nature* **613**, 479–484 (2023).
21. X. Li, J. Nan, X. Pan, Chiral induced spin selectivity as a spontaneous intertwined order. *Phys. Rev. Lett.* **125**, 263002 (2020).
22. K. Gilmore, M. D. Stiles, J. Seib, D. Steiauf, M. Fähnle, Anisotropic damping of the magnetization dynamics in Ni, Co, and Fe. *Phys. Rev. B* **81**, 174414 (2010).
23. M. Fähnle, D. Steiauf, J. Seib, The Gilbert equation revisited: Anisotropic and nonlocal damping of magnetization dynamics. *J. Phys. D Appl. Phys.* **41**, 164014 (2008).
24. S. Ghosh, B. P. Bloom, Y. Lu, D. Lamont, D. H. Waldeck, D. H., Increasing the efficiency of water splitting through spin polarization using cobalt oxide thin film catalysts. *J. Phys. Chem. C* **124**, 22610–22618 (2020).
25. J. A. Switzer, H. M. Kothari, P. Poizot, S. Nakanishi, E. W. Bohannan, Enantiospecific electrodeposition of a chiral catalyst. *Nature* **425**, 490–493 (2003).
26. S. Yakata, Y. Ando, T. Miyazaki, S. Mizukami, Temperature dependences of spin-diffusion lengths of Cu and Ru layers. *Jpn. J. Appl. Phys.* **45**, 3892 (2006).
27. R. Urban, G. Woltersdorf, B. Heinrich, Gilbert damping in single and multilayer ultrathin films: Role of interfaces in nonlocal spin dynamics. *Phys. Rev. Lett.* **87**, 217204 (2001).
28. H. Suhl, Ferromagnetic resonance in nickel ferrite between one and two kilomegacycles. *Phys. Rev.* **97**, 555–557 (1955).
29. C. Kittel, On the theory of ferromagnetic resonance absorption. *Phys. Rev.* **73**, 155–161 (1948).

30. G. M. Müller, M. Münzenberg, G. X. Miao, A. Gupta, A., Activation of additional energy dissipation processes in the magnetization dynamics of epitaxial chromium dioxide films. *Phys. Rev. B* **77**, 020412(R) (2008).
31. B. Liu, X. Ruan, Z. Wu, H. Tu, J. Du, J. Wu, X. Lu, L. He, R. Zhang, Y. Xu, Transient enhancement of magnetization damping in CoFeB film via pulsed laser excitation. *Appl. Phys. Lett.* **109**, 042401 (2016).
32. N. Li, Y.-B. Sun, R. Sun, X. Yang, W. Zhang, Z.-K. Xie, J.-N. Liu, Y. Li, Y. Li, Z.-Z. Gong, X.-Q. Zhang, W. He, Z.-H. Cheng, Topological surface state enhanced ultrafast spin dynamics of Fe/Bi_2Se_3 heterostructures. *Phys. Rev. B* **105**, 144415 (2022).
33. Y. Li, W. Zhang, N. Li, R. Sun, J. Tang, Z. Z. Gong, Y. Li, X. Yang, Z. K. Xie, Q. Gul, X. Q. Zhang, W. He, Z. H. Cheng, Optical determination of spin diffusion length and interfacial spin mixing conductance in epitaxial Pd/Fe bilayers. *J. Phys. Condens. Matter* **31**, 305802 (2019).
34. S. N. Panda, S. Mondal, J. Sinha, S. Choudhury, A. Barman, All-optical detection of interfacial spin transparency from spin pumping in β-Ta/CoFeB thin films. *Sci. Adv.* **5**, eaav7200 (2019).
35. G. Woltersdorf, M. Buess, B. Heinrich, C. H. Back, Time resolved magnetization dynamics of ultrathin Fe(001) films: Spin-pumping and two-magnon scattering. *Phys. Rev. Lett.* **95**, 037401 (2005).
36. G. Woltersdorf, B. Heinrich, B., Two-magnon scattering in a self-assembled nanoscale network of misfit dislocations. *Phys. Rev. B* **69**, 184417 (2004).
37. A. Conca, S. Keller, L. Mihalceanu, T. Kehagias, G. P. Dimitrakopulos, B. Hillebrands, E. T. Papaioannou, Study of fully epitaxial Fe/Pt bilayers for spin pumping by ferromagnetic resonance spectroscopy. *Phys. Rev. B* **93**, 134405 (2016).
38. D. Sun, K. J. van Schooten, M. Kavand, H. Malissa, C. Zhang, M. Groesbeck, C. Boehme, Z. Valy Vardeny, Inverse spin Hall effect from pulsed spin current in organic semiconductors with tunable spin-orbit coupling. *Nat. Mater.* **15**, 863–869 (2016).
39. D. V. Berkov, J. Miltat, Spin-torque driven magnetization dynamics: Micromagnetic modeling. *J. Magn. Magn. Mater.* **320**, 1238–1259 (2008).
40. R. Naaman, D. H. Waldeck, Chiral-induced spin selectivity effect. *J Phys. Chem. Lett.* **3**, 2178–2187 (2012).
41. Z.-G. Yu, Chirality-induced spin–orbit coupling, spin transport, and natural optical activity in hybrid organic–inorganic perovskites. *J Phys. Chem. Lett.* **11**, 8638–8646 (2020).
42. Y. Tserkovnyak, A. Brataas, G. E. W. Bauer, Spin pumping and magnetization dynamics in metallic multilayers. *Phys. Rev. B* **66**, 224403 (2002).
43. J. C. Rojas-Sanchez, S. Oyarzun, Y. Fu, A. Marty, C. Vergnaud, S. Gambarelli, L. Vila, M. Jamet, Y. Ohtsubo, A. Taleb-Ibrahimi, P. Le Fevre, F. Bertran, N. Reyren, J. M. George, A. Fert, Spin to charge conversion at room temperature by spin pumping into a new type of topological insulator:α-Sn films. *Phys. Rev. Lett.* **116**, 096602 (2016).
44. M. Caminale, A. Ghosh, S. Auffret, U. Ebels, K. Ollefs, F. Wilhelm, A. Rogalev, W. E. Bailey, Spin pumping damping and magnetic proximity effect in Pd and Pt spin-sink layers. *Phys. Rev. B* **94**, 014414 (2016).
45. T. Moriyama, M. Kamiya, K. Oda, K. Tanaka, K. J. Kim, T. Ono, Magnetic moment orientation-dependent spin dissipation in antiferromagnets. *Phys. Rev. Lett.* **119**, 267204 (2017).
46. L. Frangou, S. Oyarzun, S. Auffret, L. Vila, S. Gambarelli, V. Baltz, Enhanced spin pumping efficiency in antiferromagnetic IrMn thin films around the magnetic phase transition. *Phys. Rev. Lett.* **116**, 077203 (2016).
47. L. Chen, S. Mankovsky, M. Kronseder, D. Schuh, M. Prager, D. Bougeard, H. Ebert, D. Weiss, C. H. Back, Interfacial tuning of anisotropic Gilbert damping. *Phys. Rev. Lett.* **130**, 046704 (2023).
48. D. M. Polishchuk, A. Kamra, T. I. Polek, A. Brataas, V. Korenivski, Angle resolved relaxation of spin currents by antiferromagnets in spin valves. *Phys. Rev. Lett.* **123**, 247201 (2019).
49. J. Mao, Z. H. Yao, X. Zhang, J. Yun, M. Chang, Y. Zuo, L. Xi, Crystallographic direction related spin current transmission in MgO(001)/$Fe_{0.79}Si_{0.21}$(001)/Pt(111) epitaxial bilayers. *Phys. Rev. B* **103**, 134432 (2021).
50. A. A. Baker, A. I. Figueroa, C. J. Love, S. A. Cavill, T. Hesjedal, G. van der Laan, Anisotropic absorption of pure spin currents. *Phys. Rev. Lett.* **116**, 047201 (2016).
51. X. Yang, L. Qiu, Y. Li, H.-P. Xue, J.-N. Liu, R. Sun, Q.-L. Yang, X.-S. Gai, Y.-S. Wei, A. H. Comstock, D. Sun, X.-Q. Zhang, W. He, Y. Hou, Z.-H. Cheng, Anisotropic nonlocal damping in ferromagnet/α−GeTe bilayers enabled by splitting energy bands. *Phys. Rev. Lett.* **131**, 186703 (2023).
52. Y. Wolf, Y. Liu, J. Xiao, N. Park, B. Yan, Unusual spin polarization in the chirality-induced spin selectivity. *ACS Nano* **16**, 18601–18607 (2022).
53. S. Mishra, V. S. Poonia, C. Fontanesi, R. Naaman, A. M. Fleming, C. J. Burrows, Effect of oxidative damage on charge and spin transport in DNA. *J. Am. Chem. Soc.* **141**, 123–126 (2019).
54. M. C. Biesinger, B. P. Payne, A. P. Grosvenor, L. W. M. Lau, A. R. Gerson, R. S. C. Smart, Resolving surface chemical states in XPS analysis of first row transition metals, oxides and hydroxides: Cr, Mn, Fe, Co and Ni. *Appl. Surf. Sci.* **257**, 2717–2730 (2011).
55. D. H. Waldeck, R. Naaman, Y. Paltiel, The spin selectivity effect in chiral materials. *APL Mater.* **9**, 040902 (2021).
56. C. Clever, E. Wierzbinski, B. P. Bloom, Y. Lu, H. M. Grimm, S. R. Rao, W. S. Horne, D. H. Waldeck, Benchmarking chiral induced spin selectivity measurements - Towards meaningful comparisons of chiral biomolecule spin polarizations. *Isr. J. Chem.* **62**, e202200045 (2022).
57. S. Ghosh, "Chiral induced spin selectivity effect: Fundamental studies and applications," thesis, University of Pittsburgh (2021); http://d-scholarship.pitt.edu/id/eprint/40306.
58. F. Gerhardter, Y. Li, K. Baberschke, Temperature-dependent ferromagnetic-resonance study in ultrahigh vacuum: Magnetic anisotropies of thin iron films. *Phys. Rev. B* **47**, 11204–11210 (1993).
59. Y. Li, Y. Li, R. Sun, N. Li, Z.-Z. Gong, X. Yang, Z.-K. Xie, H.-L. Liu, W. He, X.-Q. Zhang, Z.-H. Cheng, Anomalous Gilbert damping induced by the coexisting static and dynamic coupling in Fe/Pd/Fe trilayers. *Phys. Rev. B* **104**, 094409 (2021).
60. J. Liu, G.-M. Choi, D. G. Cahill, Measurement of the anisotropic thermal conductivity of molybdenum disulfide by the time-resolved magneto-optic Kerr effect. *J. Appl. Phys.* **116**, 233107 (2014).
61. J. P. Feser, J. Liu, D. G. Cahill, Pump-probe measurements of the thermal conductivity tensor for materials lacking in-plane symmetry. *Rev. Sci. Instrum.* **85**, 104903 (2014).
62. W. Zhang, Q. Liu, Z. Yuan, K. Xia, W. He, Q.-f. Zhan, X.-q. Zhang, Z.-h. Cheng, Enhancement of ultrafast demagnetization rate and Gilbert damping driven by femtosecond laser-induced spin currents in $Fe_{81}Ga_{19}$/$Ir_{20}Mn_{80}$ bilayers. *Phys. Rev. B* **100**, 104412 (2019).
63. L. Zhang, Y. Hao, W. Qin, S. Xie, F. Qu, Chiral-induced spin selectivity: A polaron transport model. *Phys. Rev. B* **102**, 214303 (2020).

Acknowledgments

Funding: D.S. acknowledges the primary financial support from the Department of Energy under award number DE-SC0020992. D.S. and A.H. acknowledge the financial support from the Air Force Office of Scientific Research, Multidisciplinary University Research Initiatives (MURI) Program under award number FA9550-23-1-0311. D.H.W. acknowledges financial support from the US Department of Energy (grant no. ER46430) and the Air Force Office of Scientific Research, MURI Program under award number FA9550-23-1-0368. J.L. acknowledges financial support from the National Science Foundation under award number DMR-2011978. W.Z. acknowledges financial support from the National Science Foundation under the award number NSF-ECCS 2246254. **Author contributions:** Conceptualization: R.S., D.H.W., J.L., and D.S. Methodology: R.S., Z.W., C.Y., A.H.C., M.M., B.P.B., C.C., D.L., and A.M. Investigation: R.S., Z.W., and B.P.B. Visualization: R.S., Z.W., and B.P.B. Supervision: D.S., J.L., B.P.B., and D.H.W. Writing—original draft: R.S., B.P.B., Z.W., and D.S. Writing—review and editing: R.S., B.P.B., Z.W., D.S., D.H.W., J.L., W.Z., A.H., Z.-H.C., Z.Y., C.Y., A.H.C., M.M., C.C., D.L., and A.M. **Competing interests:** The authors declare that they have no competing interests. **Data availability:** All data needed to evaluate the conclusions in the paper are present in the paper and/or the Supplementary Materials.

Submitted 4 December 2023
Accepted 1 April 2024
Published 3 May 2024
10.1126/sciadv.adn3240